Supplementary Information

Revealing the interface-driven atomic local chemical heterogeneity in bimetallic catalysts in three dimensions

Jisheng Xie[*], Zhiheng Xie[*], Zezhou Li, Yiheng Dai, Yao Zhang, Yifan Bu, Chuhao Liu, Hong Jiang, Mufan Li[†], Jihan Zhou[†]

Beijing National Laboratory for Molecular Sciences, Center for Integrated Spectroscopy, College of Chemistry and Molecular Engineering, Peking University, Beijing, 100871, China.

[*]These authors contributed equally to this work.

[†]Correspondence and requests for materials should be addressed to to M. L. (email: mufanli@pku.edu.cn) and J. Z. (email: jhzhou@pku.edu.cn)

This PDF file includes Supplementary Table 1-6 and Supplementary Figs. 1-19.
Other Supplementary Materials for this manuscript include Supplementary Movies 1-2.

Supplementary Table 1 | Synthesis of Pd@Pt core-shell nanoparticles

Particle name	$Pd@Pt_{<1L}$	$Pd@Pt_{2L}$	$Pd@Pt_{5L}$	$Pd@Pt_{8L}$
$H_2PtCl_6 \cdot 6H_2O$ oleylamine solution (mL)	0.188	0.750	1.875	3.750

Supplementary Table 2 | Information of data collection, processing, reconstruction, angular refinement and statistics

Particle name	$Pd@Pt_{<1L}$	$Pd@Pt_{2L}$	$Pd@Pt_{5L}$	$Pd@Pt_{8L}$
Data Collection and Processing [a]				
Tilt range (°)	-76°~73.5°	-75.5°~76°	-75°~75°	-75°~75°
Electron dose (10^5 e^- $Å^{-2}$)	2.5	2.5	3.2	3.2
Refinement				
R (%) [b]	4.93	5.09	4.66	5.65
Statistics of atoms				
Total	14712	16264	21467	28357
Pd	13639	12862	13602	12439
Pt	1073	3402	7865	15918

[a] The operation parameters of all datasets are: 300 kV voltage, 30 mrad convergence semi-angle with probe size being 0.8 Å, 39.4 mrad HAADF detector inner semi-angle and 200 mrad HAADF detector outer semi-angle. The pixel size is 0.343 Å. Tilt range of all datasets are typically from -76 to 76° with number of projections being 59.

[b] Real Space Iterative Reconstruction (RESIRE) algorithm[1] was used to reconstruct each experimental tilt series, with oversampling ratio being 4 and number of iterations being 1000. R-factor is used to calculate the difference between calculated and measured projections[1].

Supplementary Table 3 | Pd/Pt atomic ratios determined by different techniques

Technique	Atomic ratio	$Pd@Pt_{<1L}$	$Pd@Pt_{2L}$	$Pd@Pt_{5L}$	$Pd@Pt_{8L}$
AET	Pd (at%)	92.7%	79.1%	63.4%	43.9%
	Pt (at%)	7.3%	20.9%	36.6%	56.1%
ICP-AES	Pd (at%)	94.5%	80.7%	61.7%	45.4%
	Pt (at%)	5.5%	19.3%	38.3%	54.6%
EDS	Pd (at%)	96.1%	83.3%	68.8%	45.6%
	Pt (at%)	3.9%	16.7%	31.2%	54.4%

Supplementary Table 4 | Result of mean bond lengths from AET

Bond type	Range	Pd@$Pt_{<1L}$	Pd@Pt_{2L}	Pd@Pt_{5L}	Pd@Pt_{8L}
All (Å)	Surface	2.82±0.08	2.80±0.10	2.80±0.08	2.77±0.07
All (Å)	Total	2.82±0.04	2.82±0.05	2.81±0.05	2.79±0.04

Supplementary Table 5 | EXAFS fitting parameters for samples at Pd K edge

Sample	CN[a]	R (Å)[b]	σ^2 ($Å^2$)[c]	ΔE_0 (eV)[d]	R-factor[e]
Pd foil	12.0*	2.74±0.002	0.0054±0.0003	7.12±0.32	0.01
Pd@$Pt_{<1L}$	11.2±0.9	2.81±0.004	0.0081±0.0006	-2.95±0.56	0.02
Pd@Pt_{2L}	11.5±1.0	2.81±0.005	0.0081±0.0006	-2.76±0.59	0.02
Pd@Pt_{5L}	11.8±1.0	2.81±0.004	0.0078±0.0005	-2.66±0.57	0.02
Pd@Pt_{8L}	11.9±1.1	2.80±0.006	0.0084±0.0007	-2.92±0.65	0.02

- S_0^2 (amplitude reduction factor) was set to be 0.80.
- a: Coordination number for the corresponding shell.
- b: Interatomic distance.
- c: Debye-Waller factors.
- d: Edge-energy shift.
- e: Goodness of fitting.
- *: This value was fixed during fitting, based on the known structure of Pd metal.
- Since atomic diameters of Pd and Pt are extremely similar, the shell in the interval of 2-3 Å includes not only the Pd-Pd but also Pd-Pt information.

Supplementary Table 6 | Result of ICP-AES for catalysts that used

Particle name	Pt/C	Pd/C	Pd@$Pt_{<1L}$/C	Pd@Pt_{2L}/C	Pd@Pt_{5L}/C	Pd@Pt_{8L}/C
Pd (wt%)	/	6.2	5.3	11.5	9.4	6.3
Pt (wt%)	52.3	/	0.6	5.0	10.7	13.9

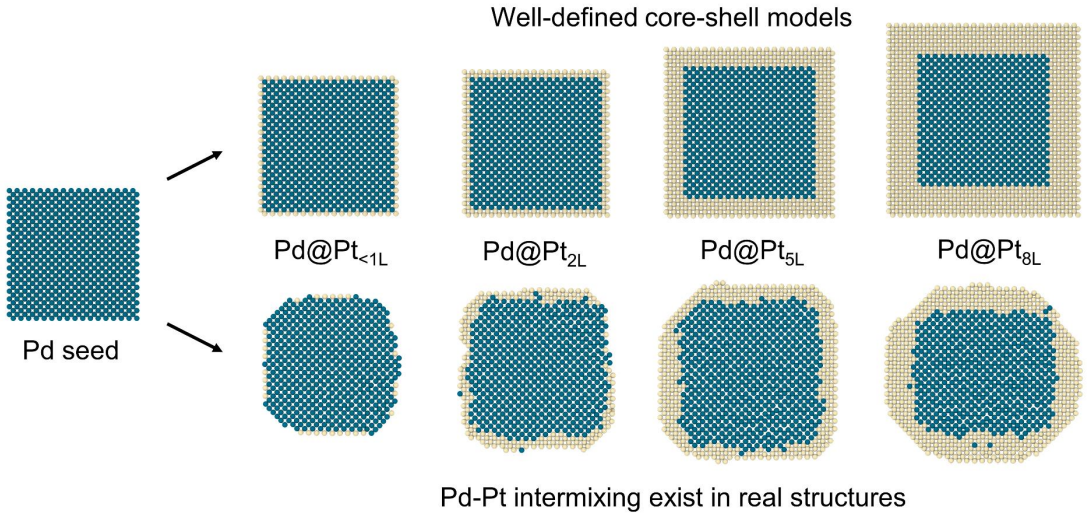

Supplementary Fig. 1 | Scheme for epitaxy growth of Pd@Pt$_{nL}$ nanoparticles in traditional cognition and in real structures. By controlling the cutoffs of interfacial diffusion of Pd atoms from core into shell, different degrees of local chemical heterogeneity were discovered on the surface of Pd@Pt$_{nL}$ nanoparticles. However, for decades, core-shell structures are treated with "well-defined" interfaces in traditional cognition, for the lack of fine-structure characterizations. Our result highlights the importance of re-consideration about the influence from subsurface to the surface structure and to the performance in electrocatalysis, not only in core-shell structures but all structures with interfaces. The structures of four Pd@Pt$_{nL}$ nanoparticles on the bottom are from the real structures we measured, after cutting central slices with one-atom thick from them.

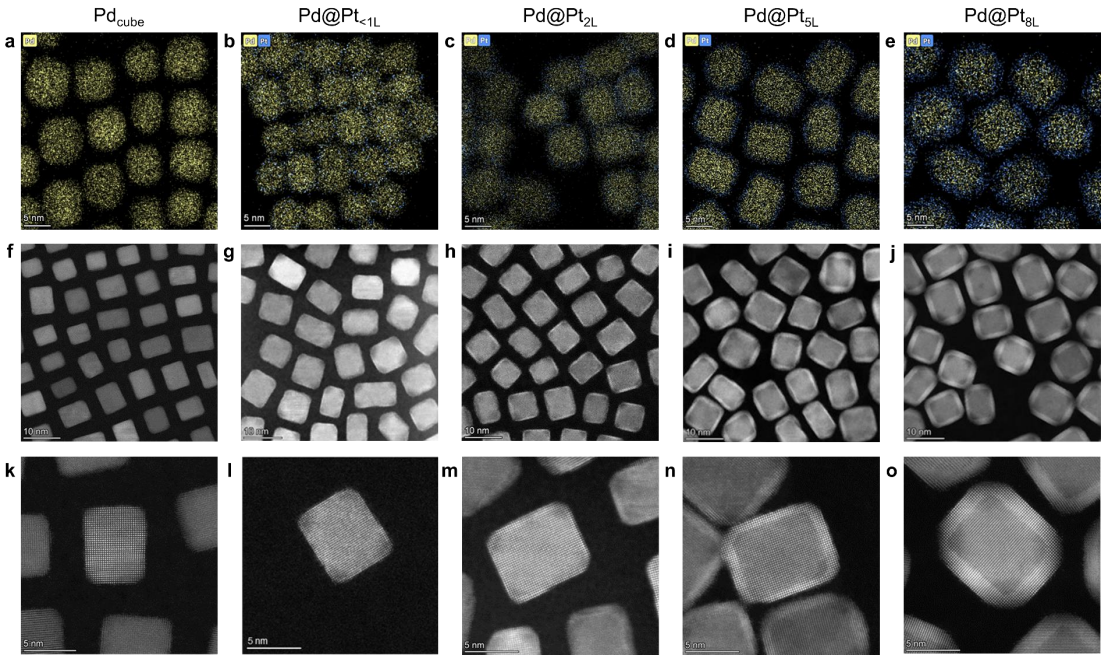

Supplementary Fig. 2 | Characterization of Pd@Pt nanoparticles. a-e, EDS mapping of Pd_{cube} seed and $Pd@Pt_{nL}$ nanoparticles. $Pd@Pt_{nL}$ nanoparticles show well-defined core-shell structures at nanometer scale. **f-o**, Atomic resolution HAADF-STEM images of Pd_{cube} seeds and $Pd@Pt_{nL}$ nanoparticles. All nanoparticles show good uniformity.

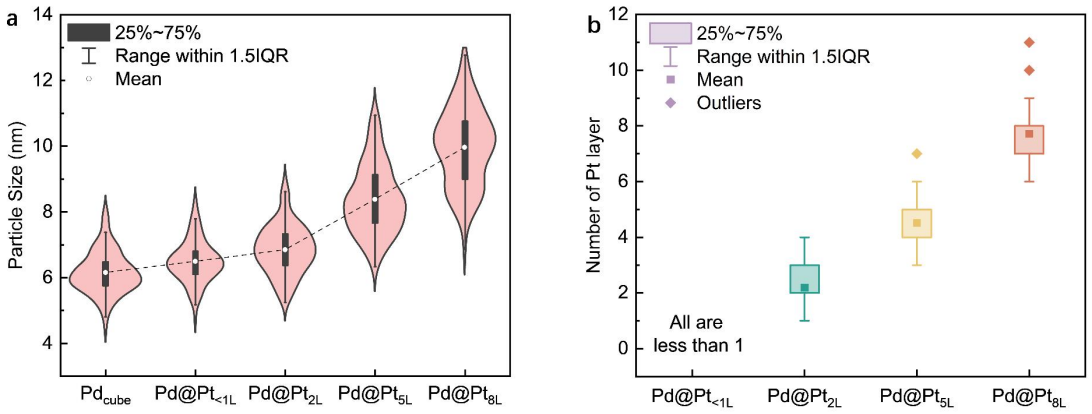

Supplementary Fig. 3 | Size distributions of Pd_{cube} and $Pd@Pt_{nL}$ nanoparticles. a, Statistics of particle sizes for Pd_{cube} and $Pd@Pt_{nL}$ nanoparticles. **b**, thicknesses of Pt shells for $Pd@Pt_{nL}$ nanoparticles. More than 100 nanoparticles were measured for the statistics of particle sizes and Pt-shell thicknesses.

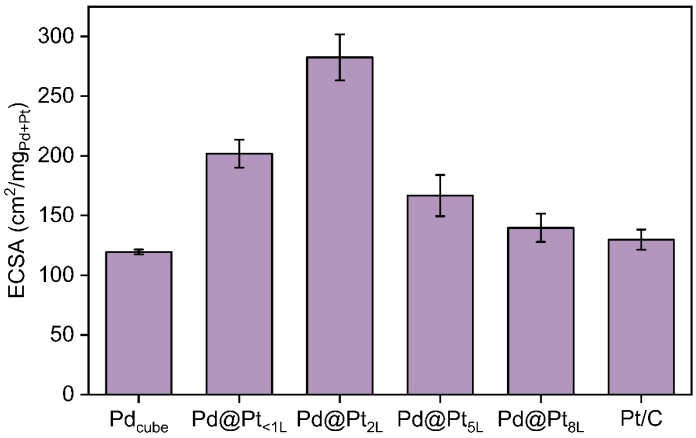

Supplementary Fig. 4 | Electrochemical active surface area of Pd/C, $Pd@Pt_{nL}$/C nanoparticles and Pt/C. The integrations of the hydrogen absorption–desorption region give ECSA of 119.5, 201.9, 282.5, 166.7, 139.7 and 129.8 cm^2/mg_{Pd+Pt} for Pd_{cube},
$Pd@Pt_{<1L}$, $Pd@Pt_{2L}$, $Pd@Pt_{5L}$, $Pd@Pt_{8L}$ and Pt/C, respectively, which indicate the adsorption behavior on surface atoms varies greatly among samples.

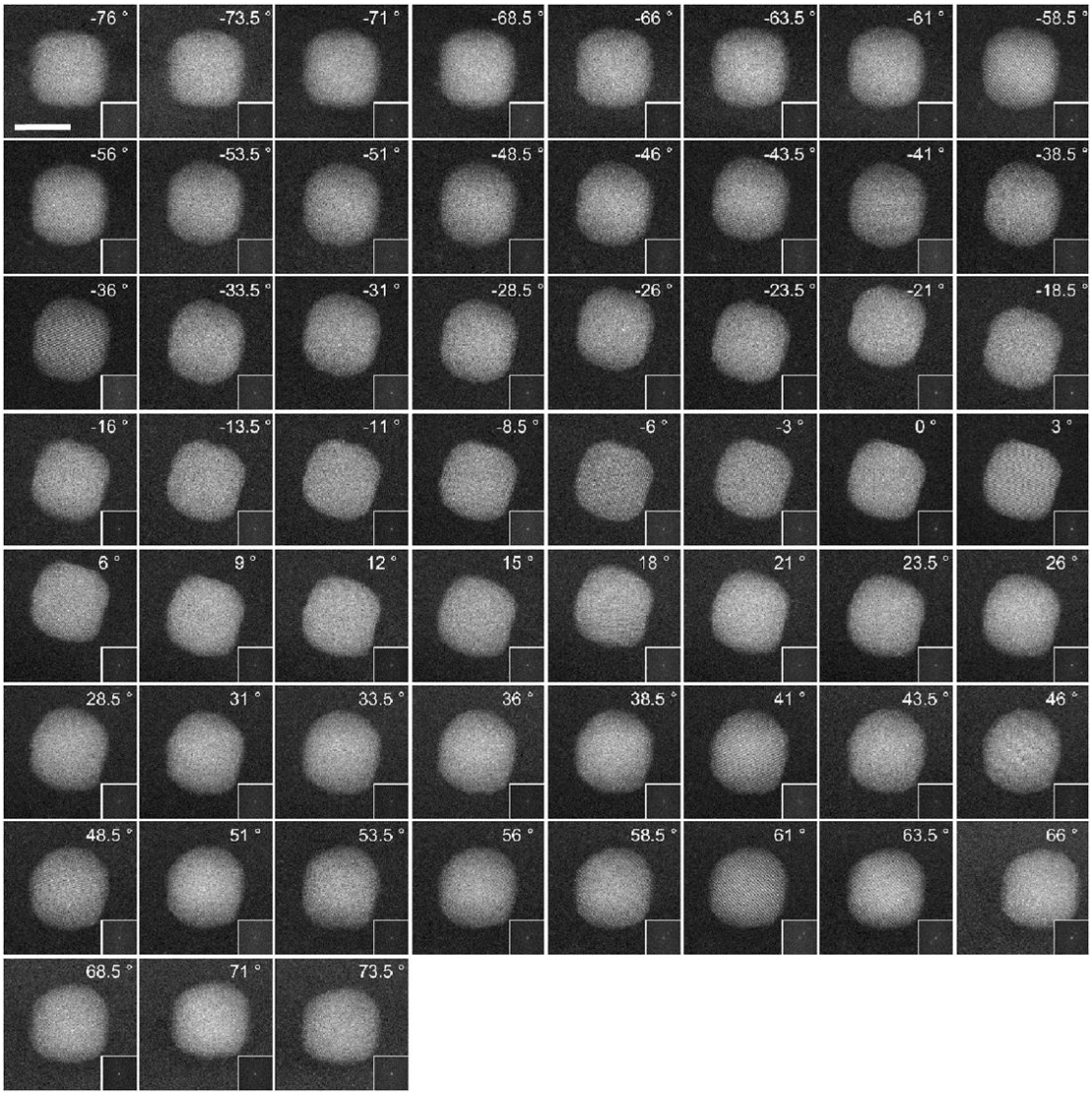

Supplementary Fig. 5 | Tomographic tilt series of Pd@Pt$_{<1L}$ nanoparticle. 59 HAADF-STEM images with a tilt range from −76.0°to +73.5°. The value of angle to which the image belongs is recorded in the upper right corner of each image. Scale bar, 2 nm.

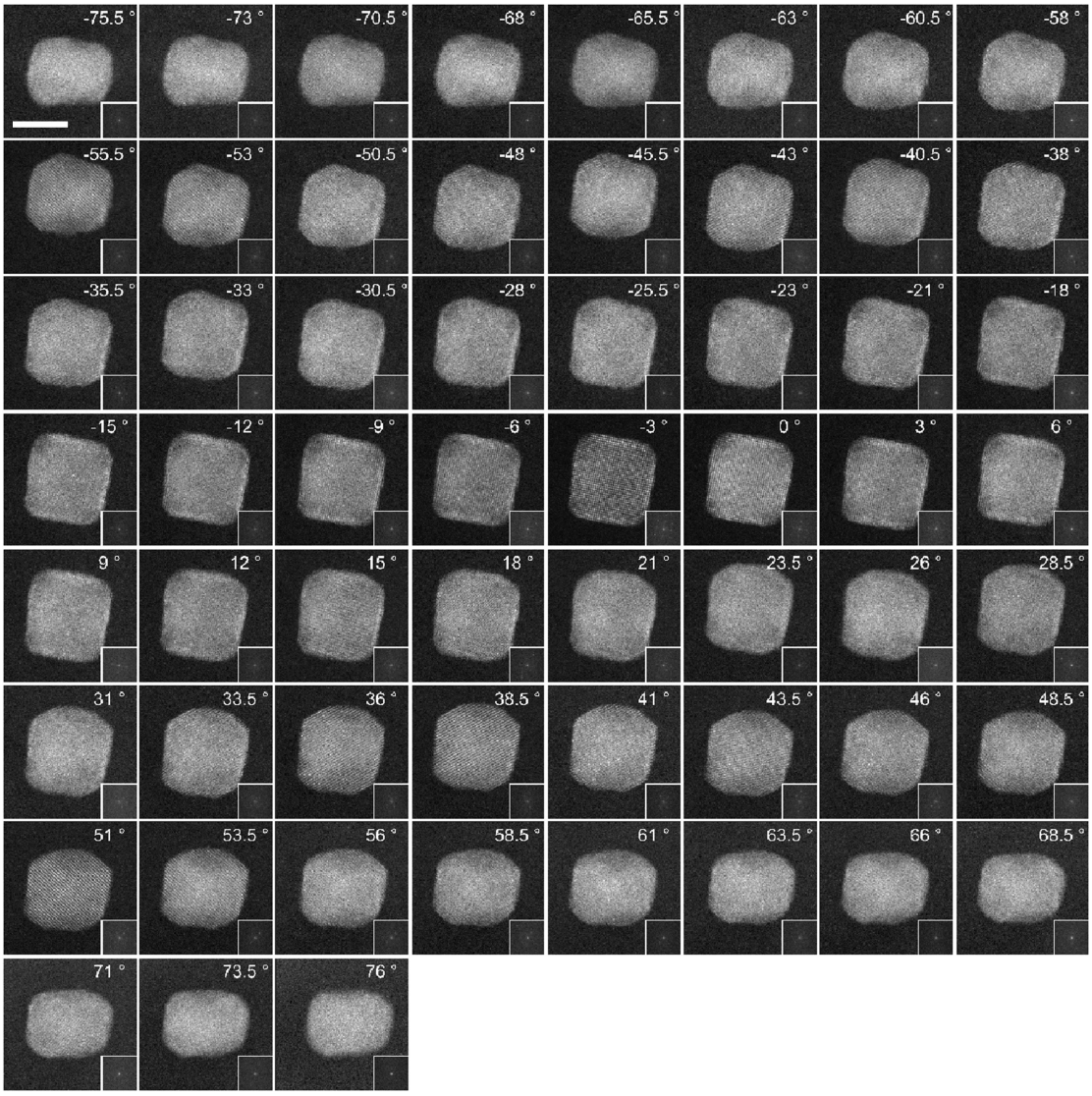

Supplementary Fig. 6 | Tomographic tilt series of Pd@Pt_{2L} nanoparticle. 59 HAADF-STEM images with a tilt range from −75.5°to +76°. The value of angle to which the image belongs is recorded in the upper right corner of each image. Scale bar, 2 nm.

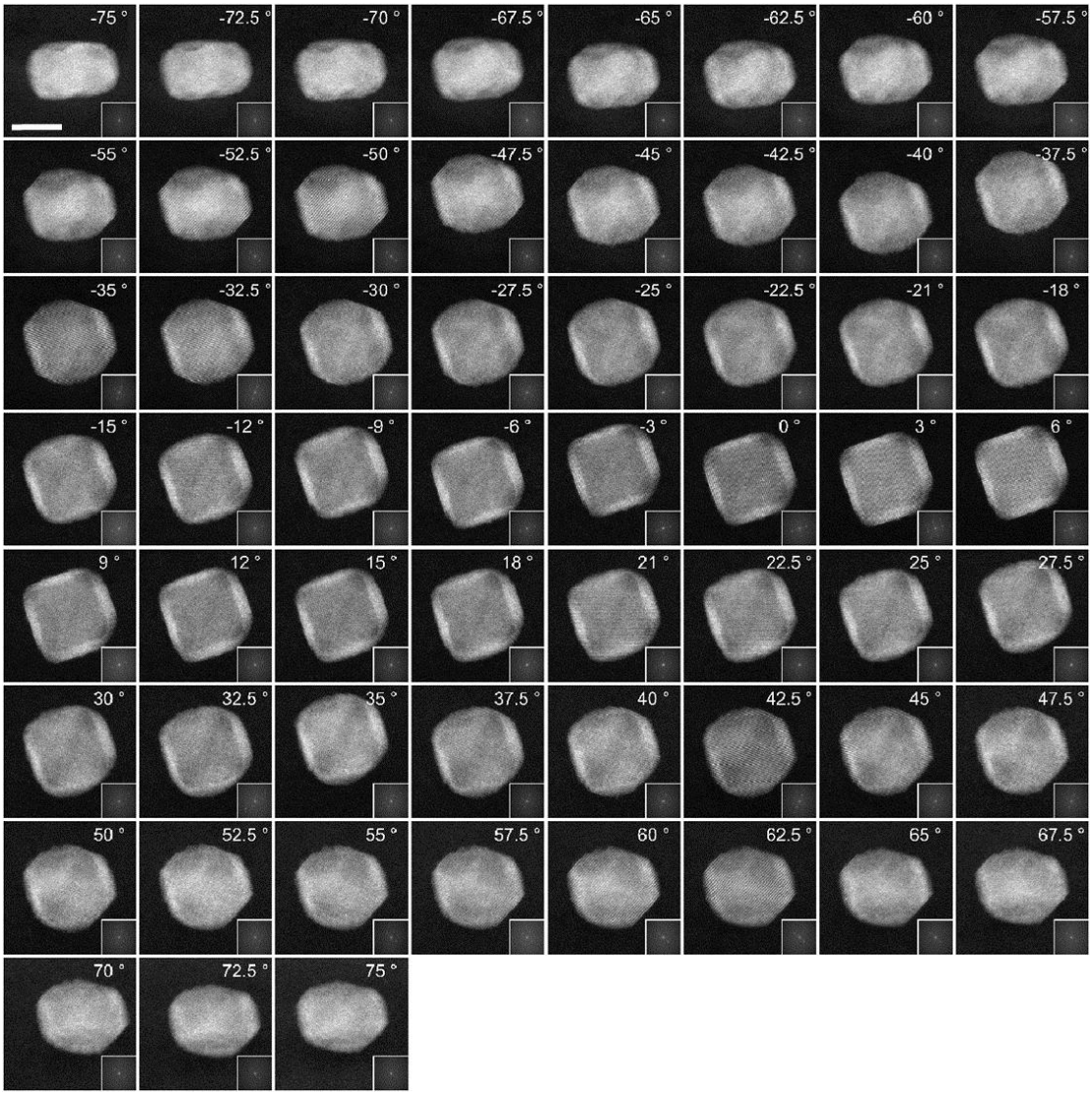

Supplementary Fig. 7 | Tomographic tilt series of Pd@Pt_{5L} nanoparticle. 59 HAADF-STEM images with a tilt range from −75.0°to +75.0°. The value of angle to which the image belongs is recorded in the upper right corner of each image. Scale bar, 2 nm.

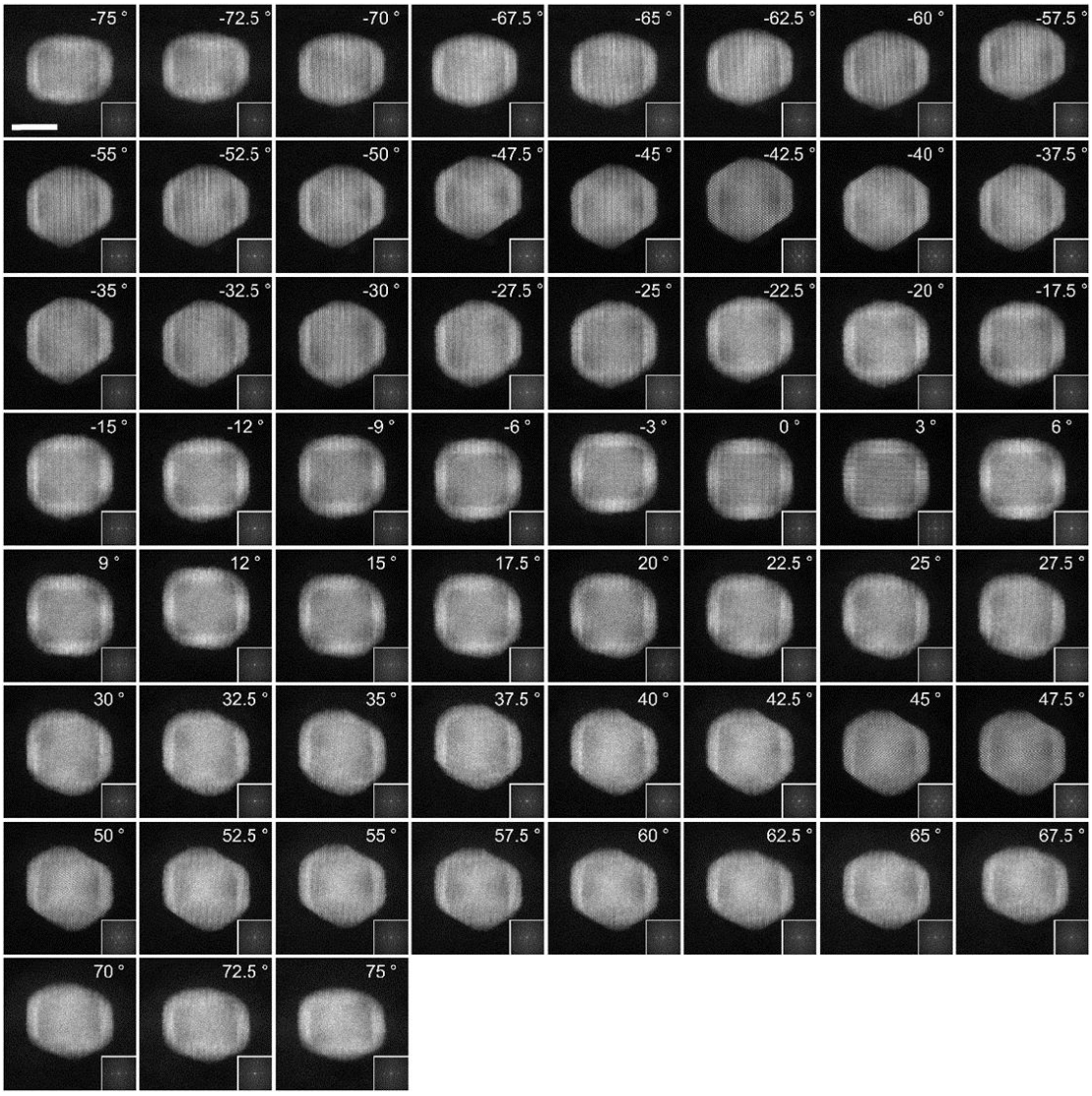

Supplementary Fig. 8 | Tomographic tilt series of Pd@Pt$_{8L}$ nanoparticle. 59 HAADF-STEM images with a tilt range from −75.0°to +75.0°. The value of angle to which the image belongs is recorded in the upper right corner of each image. Scale bar, 2 nm.

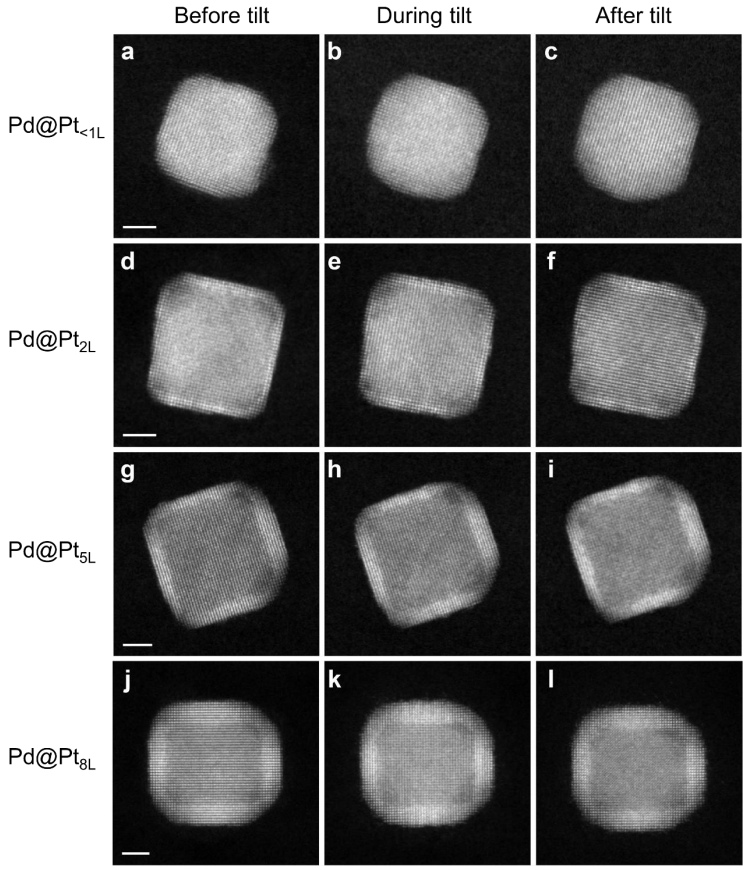

Supplementary Fig. 9 | Consistency check of Pd@Pt$_{nL}$ nanoparticles. 0° projection images of Pd@Pt$_{<1L}$ (**a-c**), Pd@Pt$_{2L}$ (**d-f**), Pd@Pt$_{5L}$ (**g-i**) and Pd@Pt$_{8L}$ (**j-l**) before (**a**, **d**, **g** and **j**), during (**b**, **e**, **h** and **k**) and after (**c**, **f**, **i** and **l**) tilting experiments.

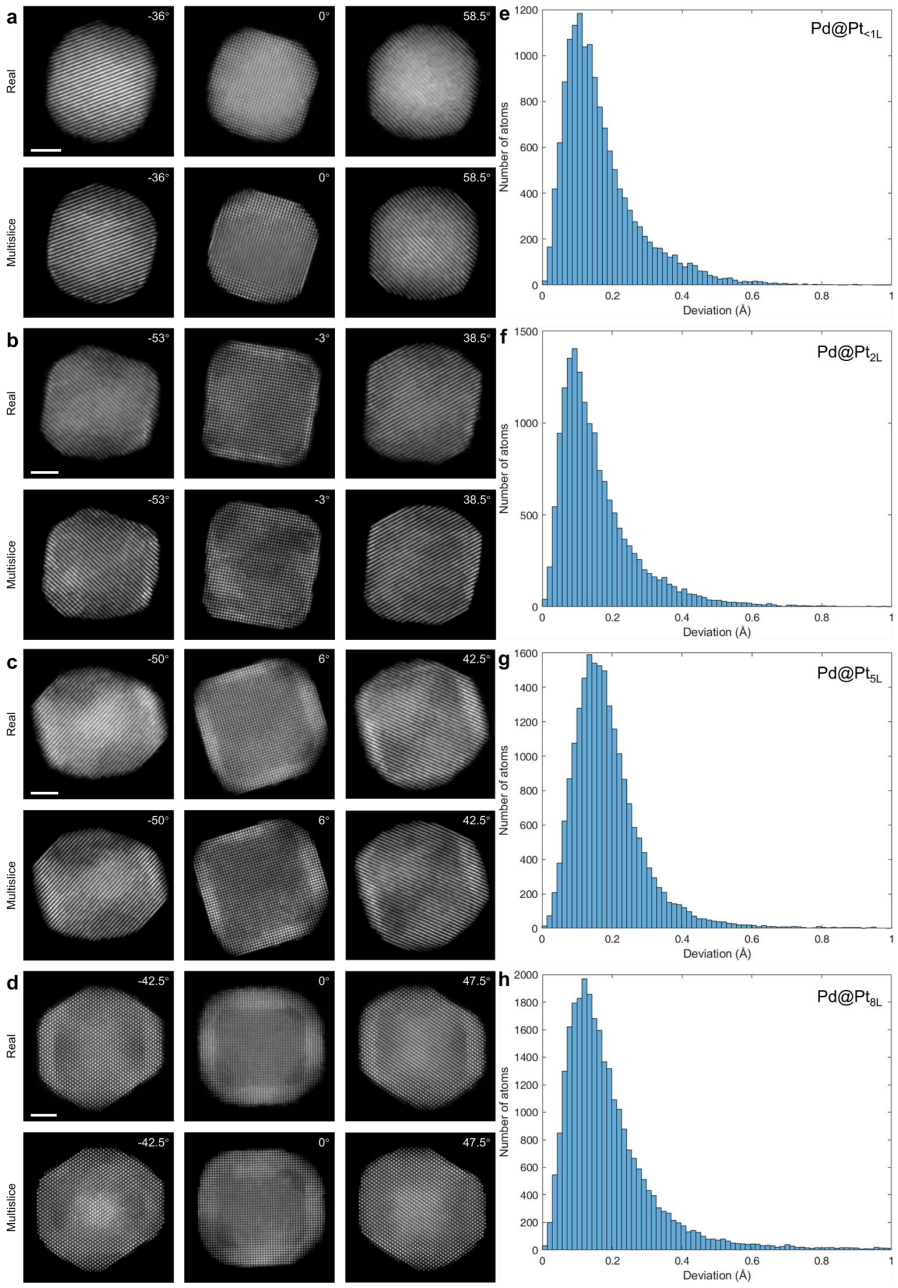

Supplementary Fig. 10 | Validation of the reconstructions of Pd@Pt$_{nL}$ nanoparticles using multi-slice simulation. a-d, Comparison between experimental images and multi-slice simulation images for Pd@Pt$_{<1L}$ (**a**), Pd@Pt$_{2L}$ (**b**), Pd@Pt$_{5L}$ (**c**), and Pd@Pt$_{8L}$ (**d**), respectively, which are in good agreement with the corresponding experimental images. All multi-slice simulation images are calculated from the experimental 3D atomic coordinates. The value of angle to which the image belongs is recorded in the upper right corner of each image. Scale bar in **a-d**, 2 nm. **e-h**, Histogram of the root-mean-square deviation (RMSD) between experimental and simulated 3D atomic coordinates traced from reconstructions of Pd@Pt$_{<1L}$ (**e**), Pd@Pt$_{2L}$ (**f**), Pd@Pt$_{5L}$ (**g**), and Pd@Pt$_{8L}$ (**h**), respectively. RMSD of all common atom pairs were 20 pm (**a**, **e**, Pd@Pt$_{<1L}$) with 99.3% atoms traced, 20 pm (**b**, **f**, Pd@Pt$_{2L}$) with 99.2% atoms traced, 22 pm (**c**, **g**, Pd@Pt$_{5L}$) with 98.5 % atoms traced and 27 pm (**d**, **h**, Pd@Pt$_{8L}$) with 97.7% atoms traced, respectively.

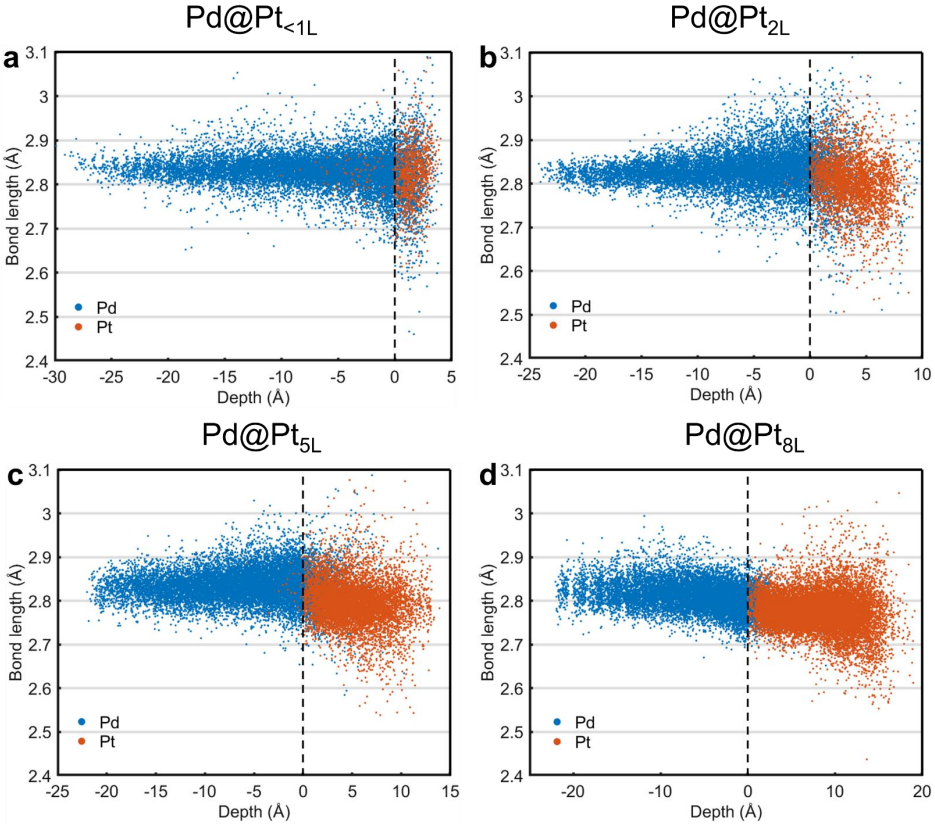

Supplementary Fig. 11 | Bond length statistics with depth of Pd@Pt$_{nL}$ NPs using AET. a-d, Distribution of bond length versus depth in Pd@Pt$_{nL}$ nanoparticles. Zero depth (red line) is defined at the surfaces of Pd cores in each nanoparticle.

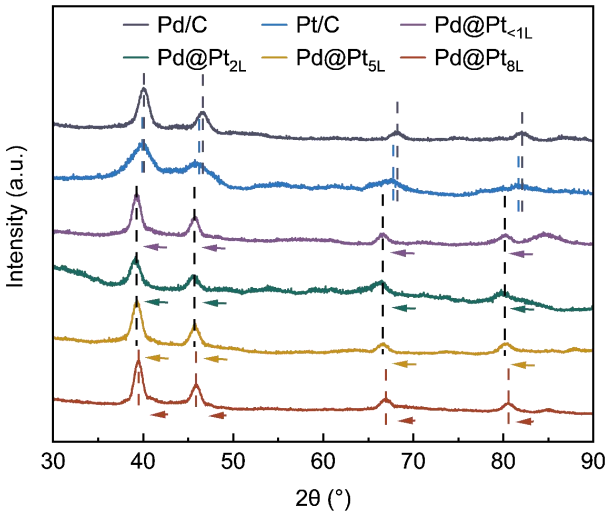

Supplementary Fig. 12 | PXRD patterns of Pd/C, Pt/C and Pd@Pt$_{nL}$/C nanoparticles. XRD patterns of Pd@Pt$_{nL}$ CS-NPs show two diffraction peaks at around 40°, 46°, 67°and 81°, assigned to the {111}, {200}, {220} and {311} planes in face centered cubic (FCC) crystalline, respectively. The average bond lengths are 2.81 Å, 2.81 Å, 2.80 Å and 2.79 Å for Pd@Pt$_{<1L}$ Pd@Pt$_{2L}$, Pd@Pt$_{5L}$ and Pd@Pt$_{8L}$, respectively.

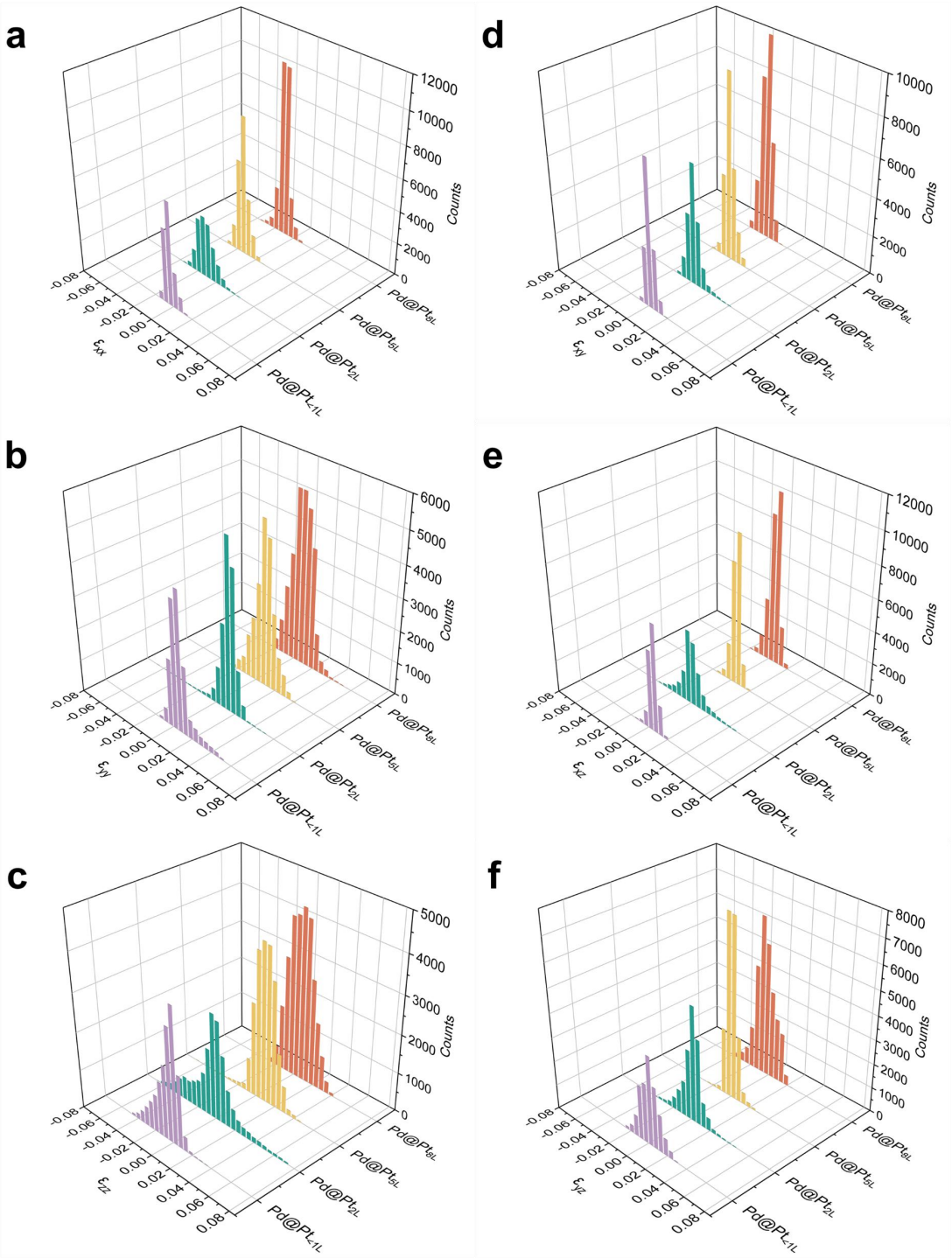

Supplementary Fig. 13 | 3D strain tensor analysis of Pd@Pt$_{nL}$ nanoparticles. a-f Statistics of six components of full strain tensors for total atoms of Pd@Pt$_{nL}$ nanoparticles in the direction of ε_{xx}, ε_{yy}, ε_{zz}, ε_{xy}, ε_{xz} and ε_{yz}, respectively.

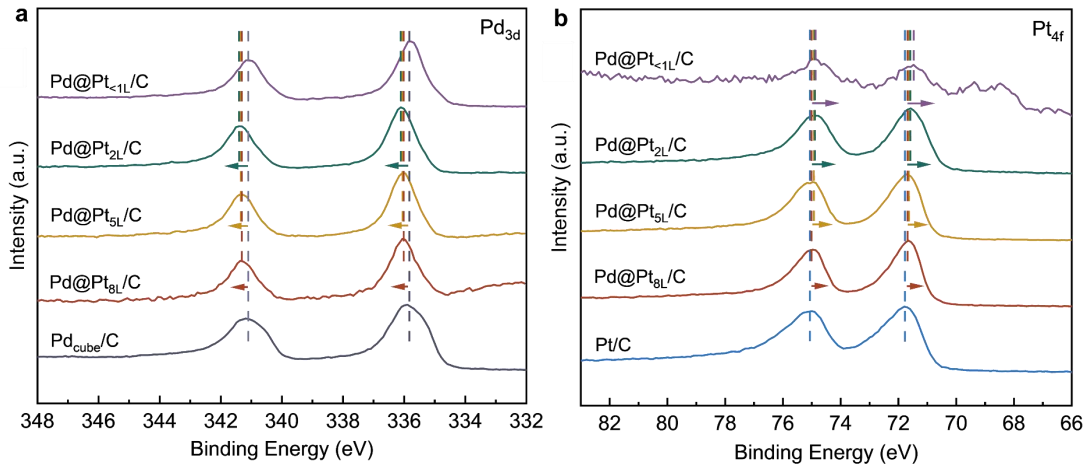

Supplementary Fig. 14 | Results of XPS spectra. a Pd 3*d* XPS spectra of Pd@Pt_{nL}/C nanoparticles and Pd/C. Pd 3d binding energy in Pd@Pt_{nL} CS-NPs shift positively as Pd@Pt_{8L}, Pd@Pt_{5L} and Pd@Pt_{2L}, while Pd@$Pt_{<1L}$ shows the lowest binding energy. **b** Pt 4*f* XPS spectra of Pd@Pt_{nL}/C nanoparticles and Pt/C. The Pt 4f binding energy in Pd@Pt_{nL} NPs shift negatively as Pd@Pt_{8L}, Pd@Pt_{5L} and Pd@Pt_{2L}, while increased in Pd@$Pt_{<1L}$. The abnormal decreasing of Pd 3d binding energy and increasing of Pt 4f binding energy in Pd@$Pt_{<1L}$can be attributed to the lowest Pt/Pd ratio among Pd@Pt_{nL} NPs, which corresponds to the weakest Pd/Pt interactions, consistent with the AET result.

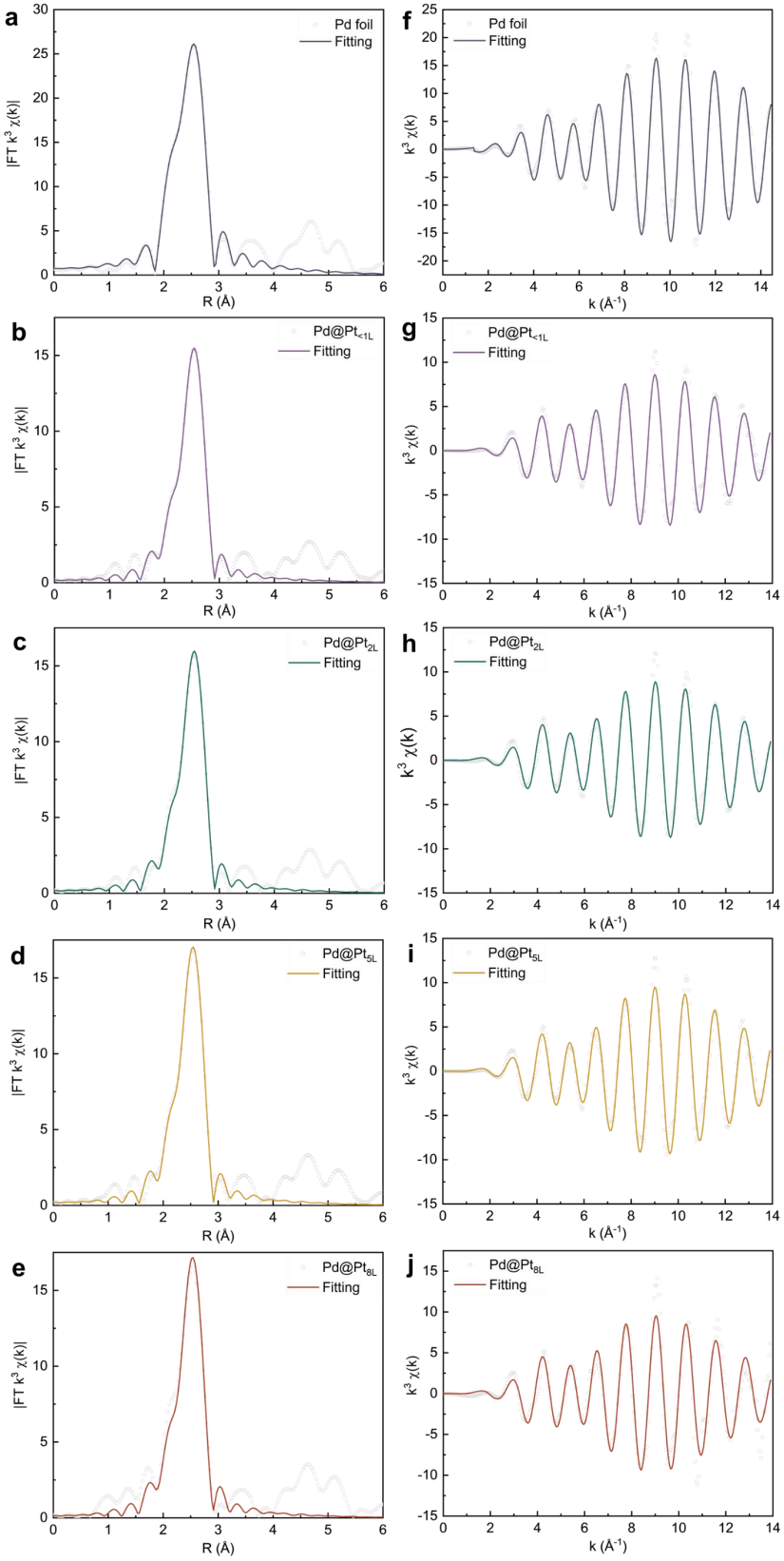

Supplementary Fig. 15 | Fitting results of FT-EXAFS. The *R* space (**a-e**) and *k* space (**f-j**) fitting results of Pd *K*-edge for (a, f) Pd foil, (b, g) Pd@Pt<1L/C, (c, h) Pd@Pt2L/C, (d-i) Pd@Pt5L/C and (e, j) Pd@Pt8L/C, respectively.

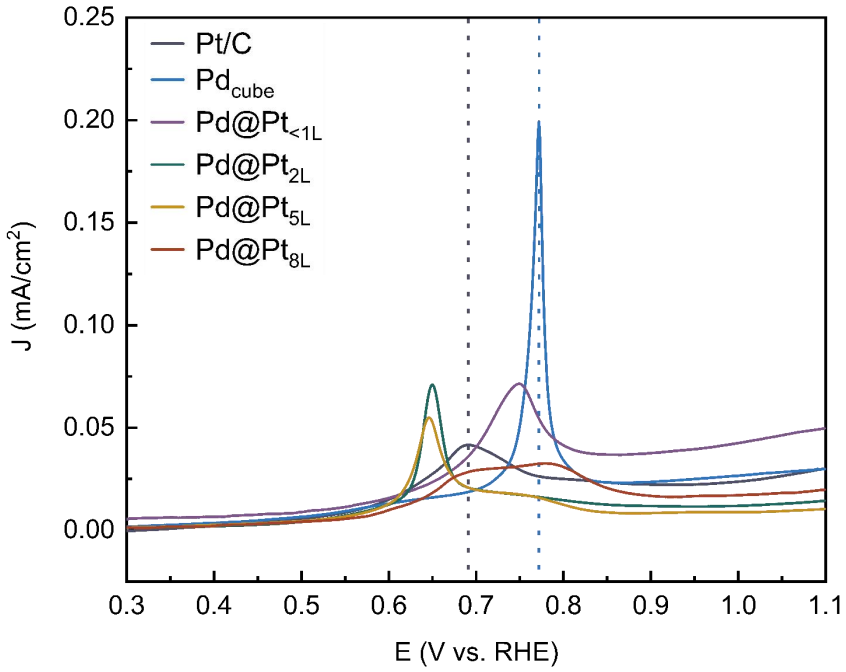

Supplementary Fig. 16 | Electrochemical desorption curve of CO for Pt/C, Pd_{cube} and $Pd@Pt_{nL}$ nanoparticles.

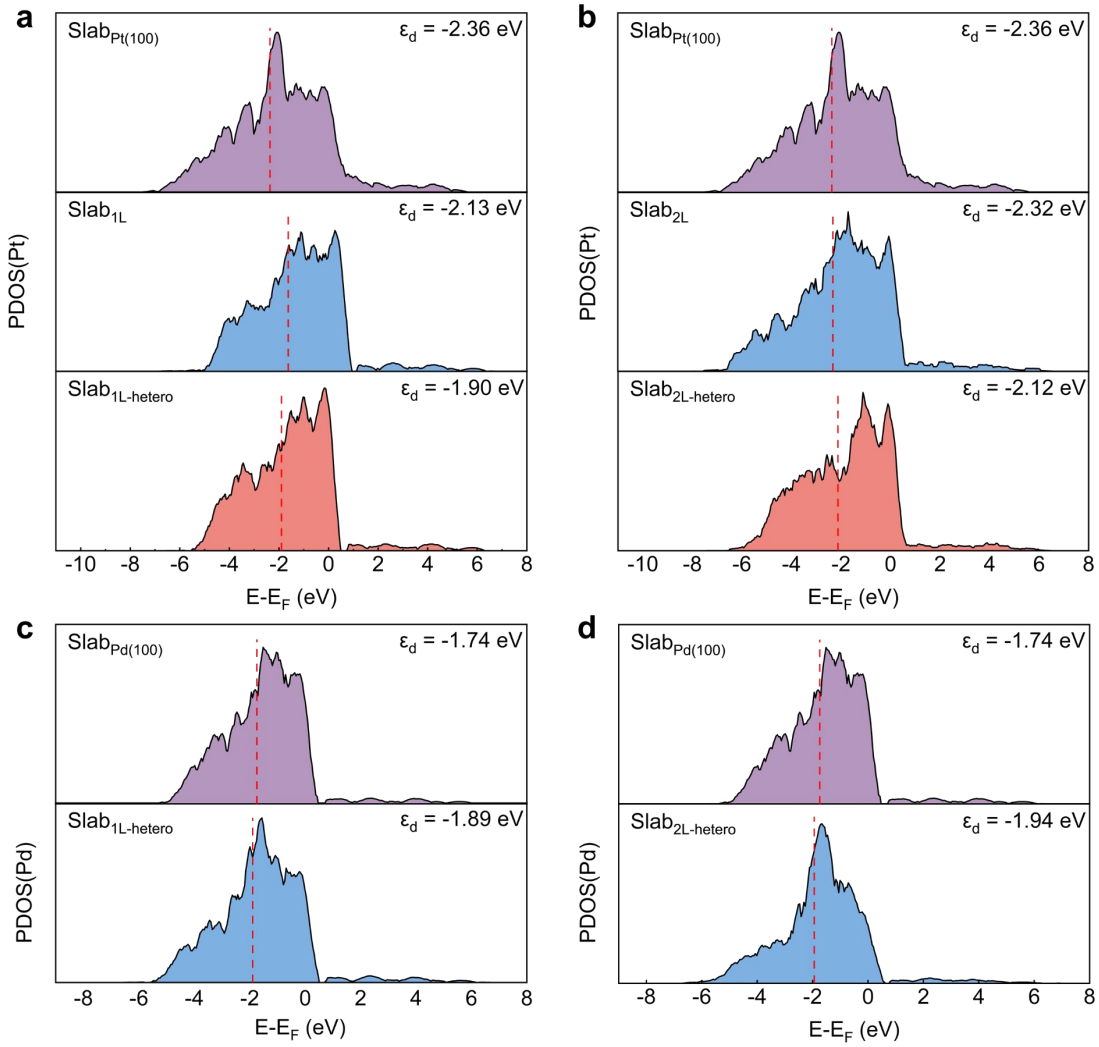

Supplementary Fig. 17 | Supporting projected density of states calculation of slab models. The projected density of states of slab models for $Slab_{Pd(100)}$, $Slab_{1L}$ and $Slab_{1L\text{-}hetero}$ on Pt d-orbital (**a**), $Slab_{Pd(100)}$, $Slab_{2L}$ and $Slab_{2L\text{-}hetero}$ on Pt d-orbital (**b**), $Slab_{Pd(100)}$ and $Slab_{1L\text{-}hetero}$ on Pd d-orbital (**c**), $Slab_{Pd(100)}$ and $Slab_{2L\text{-}hetero}$ on Pd d-orbital (**d**).

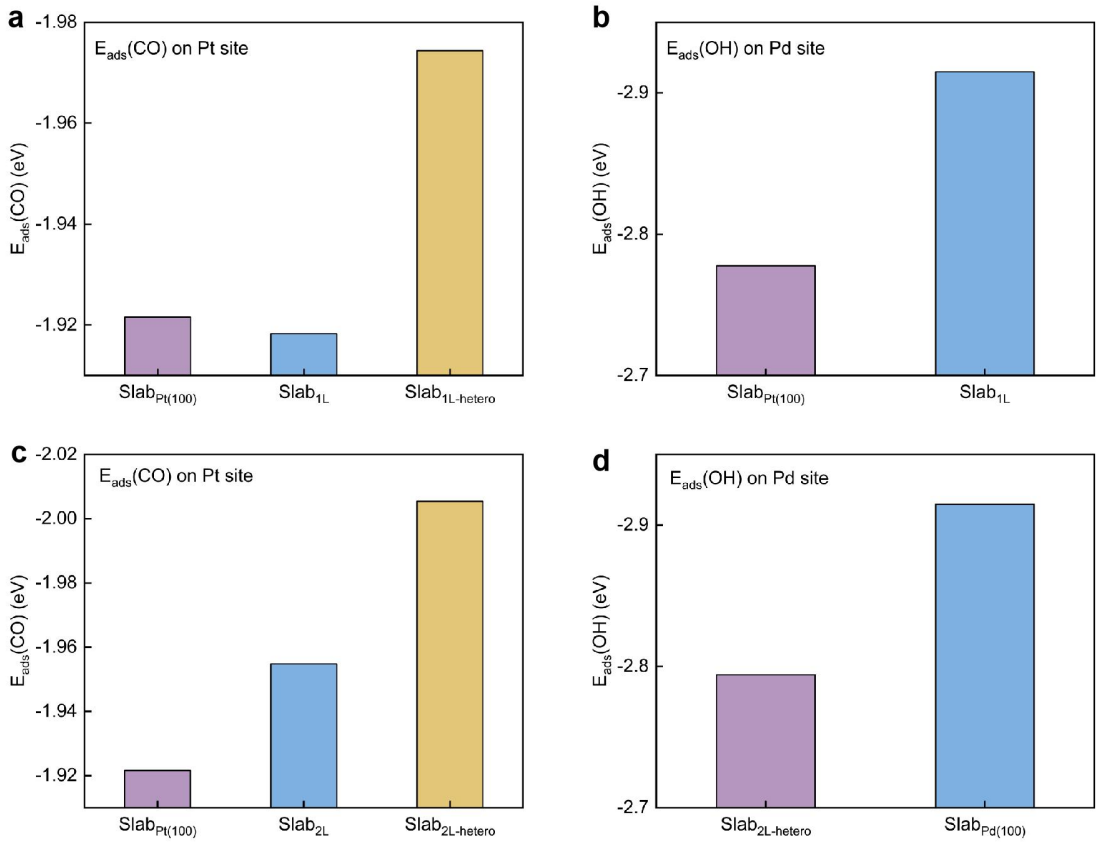

Supplementary Fig. 18 | Supporting DFT calculation of Pd@Pt_{nL} nanoparticles. a-b The calculated CO adsorption energy (E_{ads} (CO)) on surface Pt atop sites (a) and OH adsorption energy (E_{ads} (OH)) on surface Pd atop sites (b) of $Slab_{Pd(100)}$, $Slab_{1L}$ and $Slab_{1L\text{-}hetero}$. **c-d** The calculated CO adsorption energy (E_{ads} (CO)) on surface Pt atop sites (a) and OH adsorption energy (E_{ads} (OH)) on surface Pd atop sites (b) of $Slab_{Pd(100)}$, $Slab_{2L}$ and $Slab_{2L\text{-}hetero}$.

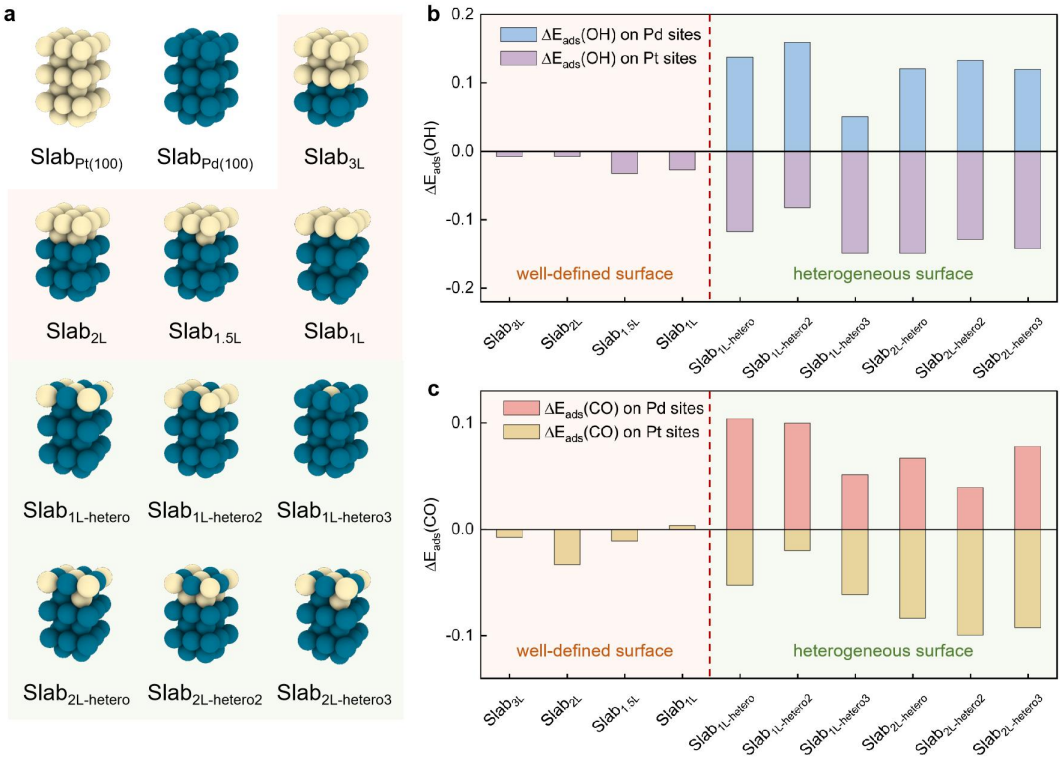

Supplementary Fig. 19 | Additional adsorption energies calculation for more slab models with local chemical heterogeneity. a The slab models for pure Pd and Pt slab, Pd@Pt slab models with will-defined surface (in red panel) and Pd@Pt slab models with heterogeneous surface (in green panel). **b-c** The adsorption energies of OH and CO for additional slab models. For models of Pd@Pt with will-defined surface, both adsorption energies has little difference with pure mental slab (<0.05 eV). For most models with heterogeneous surface, E_{ads}(OH) on Pt sites are much lower and E_{ads}(CO) on Pd sites are much higher than pure metal slab, indicating the promote of OH adsorption and weaken effect of CO adsorption on heterogeneous surface. The corresponding adsorption energies on Pd sites terms are blank, for there is no surface Pd atoms on the models with will-defined surface. ΔE_{ads}(X-M) is defined as difference between E_{ads}(X) on metal *M* site for models and E_{ads}(X) on metal *M* site for pure metal model.

Reference

1. Pham, M., Yuan, Y., Rana, A., Osher, S. & Miao, J. Accurate real space iterative reconstruction (RESIRE) algorithm for tomography. *Sci. Rep.* **13**, 5624 (2023).